DIRECT ATOMIC IMAGING OF SOLID SURFACES
I. Image simulation and interpretation

L.D. MARKS *

Cavendish Laboratory, Department of Physics, University of Cambridge, Madingley Road, Cambridge CB3 OHE, UK

This paper describes some of the more important features of high resolution electron image simulation and interpretation necessary for the detailed interpretation of experimental micrographs of solid surfaces at the atomic level. The emphasis is upon theoretical image simulations, but a number of experimental images are included for comparison. In detail, the mechanics of setting up the calculations without introducing unwanted interference between surfaces, the role of localisation in obtaining images which are representative of the local surface structure and the imaging effects of a surface potential, relaxations, reconstructions and contaminant superstructures are briefly discussed and the qualitative effects expected for somewhat thicker specimens are considered.

1. Introduction

The last few years have seen substantial progress in the application of electron microscope imaging techniques to the field of surface science. Employing either the experimental configuration used for reflection high energy electron diffraction (RHEED) (e.g. refs. [1,2]), or transmitted beams which are surface sensitive (e.g. ref. [3]) it has proved possible to obtain extensive real space information. For instance, the phase transition between the Si(111) 1×1 and 7×7 surfaces has been observed to nucleate at surface steps [2]. These techniques use the variation with position of the intensity of a surface sensitive diffracted beam to form low resolution (~ 2 nm) images. A further technique in electron microscopy, namely high resolution imaging, is capable of providing direct information on the scale of the atomic structure. The approach is to employ the low order diffracted beams to produce an interference image which (under appropriate conditions) represents the atomic structure of the material under investigation. (For a recent review see ref. [4], and a discussion of many of the experimental and theoretical aspects can be found in the book by Spence [5].)

---

* Present address: Department of Physics, Arizona State University, Tempe, Arizona 85281, USA

Early work (not specifically concentrating on surfaces) implied that surface information was accessible by high resolution electron microscopy, for example the observation of spacing variations in narrow graphite ribbons by Iijima [6], and a MoS_2 phase on the surface of a MoO_2 catalyst by Sanders [7]. More recent results [8–13] have demonstrated that this technique can directly reveal the atomic structure of surfaces. Employing small metal particles of typical diameter 20 nm oriented down a $\langle 110 \rangle$ pole with the electron beam grazing the surface of interest, and more recently large crystallographic holes in continuous films with in-situ cleaning [13], detailed information on surface steps, facetting and surface reconstructions has been obtained. (See fig. 1 and refs. [8,10].) For instance, it has proved possible to detail the atomic structure of the gold (110) 2×1 surface, including measurement of a $20 \pm 5\%$ outward relaxation for some of the atoms [9].

Unfortunately, high resolution electron microscope images can be misleading. Since the experimental results are pictures, it is possible to fall into the psychological trap of interpreting the results of a complicated diffraction and aberration limited imaging process in the same manner as our eyes interpret the everyday world (seeing is believing). This can be totally wrong, and it is necessary to numerically compute the images to determine how and with what confidence the experimental images should be interpreted. The intention of this paper is to describe recent theoretical work on atomic imaging of surfaces, concentrating on interpreting the images using numerically calculated images but including a number of illustrative experimental images obtained from small gold particles or continuous films (part of a joint collaborative project
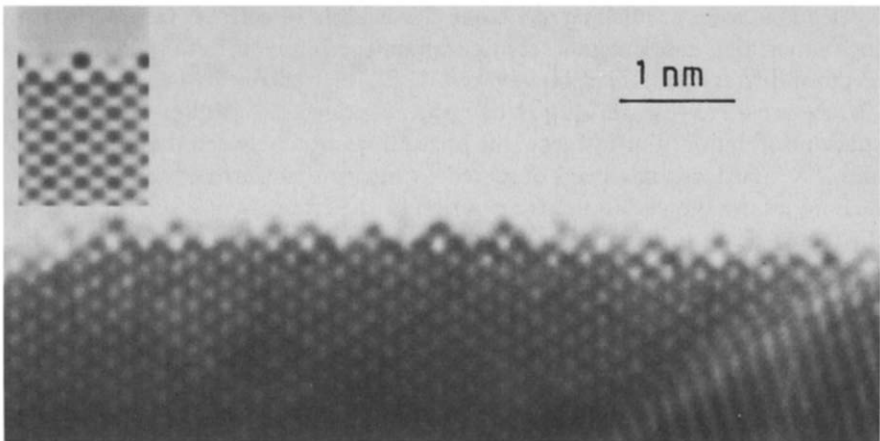

Fig. 1. Image of an area of gold (110) surface showing a region of partially reconstructed 2×1 surface [9]. Inset is an image simulation with a $23\frac{1}{2}\%$ outward relaxation at the top of the serrated structure and a 10% occupancy of the channels.

with Dr. D.J. Smith [8–13]). No attempt is made to provide an exhaustive summary, only to discuss some of the more important aspects. In section 2 the mechanics of the calculations are briefly described, the importance of localisation in the images is discussed in section 3, whilst section 4 discusses briefly the effects of a surface potential, steps, relaxations, reconstructions and impurities. Section 5 considers the type of qualitative effects that can be expected for rather thick crystals as these are likely to be rather different than for thin crystals. Applications of the theoretical image calculations will be discussed elsewhere [9–13], together with the experimental results.

2. Numerical methods

The numerical multislice [14–16] calculations were carried out using a suite of programs originating from Melbourne (courtesy of Dr. G.J. Woods), modified to include virtual array memory. Instrumental parameters for the Cambridge microscope [17] were a C_s of 2.7 mm at 500 kV, a focal spread half width of 16 nm and incident beam convergences of about 0.3–0.5 mrad, the latter two being included by an incoherent summation in the image plane. (Use of a reciprocal space convolution [18–20] was avoided as it contains an implicit approximation that the scattering is independent of the incident electron beam direction over the convergence of the condensor aperture, which may be invalid for a surface when beams can be reflected.) A small cell dimension (x axis) was employed in the surface plane (exploiting the periodic continuation implicit in the technique to extend the crystal), and a large dimension (y axis) normal to the surface as shown in fig. 2.
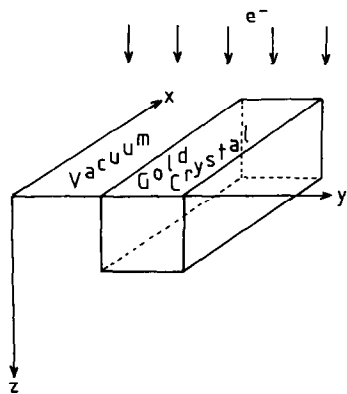

Fig. 2. Diagram to show the axes and unit cell employed for the calculations (not to scale). The y dimension was in general 32 times as large as the x dimension.

One major problem with a surface calculation is the cell size; the y dimension must be large enough to prevent unwanted interference during the electron scattering or electron optical imaging which can arise because numerical Fast Fourier Transforms implicitly periodically extend the unit cell. Transverse spreading of the diffracted beams can be estimated as $\Delta y = t\theta_{max}$, where t is the thickness and θ_{max} the maximum diffraction angle. For $t = 10$ nm and $\theta_{max} = 50$ mrad, $\Delta y = 0.5$ nm. (θ_{max} will depend upon the electron voltage and for 100 kV a substantially larger value would be required.) For imaging, the spherical aberration must be included and for high angle scattering $\Delta y = C_s\theta_{max}^3$. Taking $C_s = 2$ mm, $\Delta y = 50$ nm. However, it is unnecessary to employ a surface clearance of this order for three reasons. Firstly, the intensity in beams with large scattering angles is very small (for a thin specimen), so the magnitude of any error from their exclusion is small. Secondly, this spreading is strictly a translation, and in the experimental images the contribution (at the surface) from any high angle beams will originate from some region of the specimen where the thickness may be totally different. Finally, these high angle beams only contribute to the background level, not the lattice fringe structure, and knowledge of their intensity in the images is not necessary for quantitative analyses of the surface structure. Hence it is justifiable to exclude these high angle beams from the calculated images with an aperture accepting a small error in the background intensity. (There are also uncertainties in the background level due to inelastic scattering, for which no satisfactory computational approach yet exists, which will probably be of similar order.) For small angle scattering with a defocus Δz the displacement is $\Delta y = \Delta z \, \theta + 2C_s\theta^3$, so for a typical value for 500 kV incident electrons of $\theta = 10^{-2}$, for Gaussian defocus ($\Delta z = 0$), $\Delta y = 1$ nm. For surface calculations a y dimension of about 4 nm half occupied by crystal, giving a separation between the surfaces of about 2 nm, has proved adequate (for 500 kV electrons and $C_s = 2.7$ mm). However, these values are microscope-dependent and for 100 kV will almost certainly need to be doubled.

The multislice technique requires that the slice thickness be sufficiently small and the number of scattered beams large enough for the calculation to converge [14,15]. For gold down the (110) direction at 500 kV the required slice was $\frac{1}{4}$(110) (1.45 Å), with beams out to 10 Å^{-1} included in the calculation, although it was possible to obtain reasonable results with twice the slice thickness and half the reciprocal space sampling. These did not give accurate quantitative results, but the qualitative images were generally accurate enough to rule out many hypothetical surface structures. Calculations for other than a simple 1×1 structure can introduce excessive demands upon computer store. The conventional technique for avoiding this type of problem is to employ virtual memory, but for a multislice calculation this approach is intractable; the technique depends heavily upon Fast Fourier Transform algorithms, and the standard two-dimensional Cooley–Tukey method [21] is not suitable for

virtual memory – it becomes excessively slow. To overcome this, an algorithm employing one-dimensional Fast Fourier transforms with a buffered array transpose was developed, which is described for reference in the appendix.

3. Localisation and the column approximation

In order to gauge how useful high resolution electron microscopy images of surfaces are, it is necessary to understand what distortions the diffraction and electron optical imaging introduce. Ideally the image should be a one to one map of the object with the signal from each column of atoms independent. Both the diffraction and the imaging can instead lead to a final image representing some form of positional average, in general the imaging being more important.

The scattering from each column of atoms should be independent, equivalent to the so called column approximation [22], and the conditions for this have been analysed in some detail in the literature. Inside a crystal the electron wave can be expanded about scattering eigenfunctions (Bloch waves) which propagate independently. Down a high symmetry zone axis these waves are highly localised around the atomic cores (e.g. refs. [23,24]), with relatively little cross-talk between different columns. (This effect which is known as channelling becomes more marked both as the incident electron energy increase and with stronger scattering potentials.) For typical specimen thicknesses (< 10 nm) and down a zone axis the scattering from different columns of atoms is to a good approximation independent. Effects arising for thicker crystals or off the zone axis when this is not true are briefly discussed in section 5.

Far more serious are the effects of the microscope aberrations; compared to a light microscope, an electron microscope is a series of highly imperfect lenses. It is necessary to consider the effects of the spherical aberration, objective lens defocus and terms such as the incident beam convergence and chromatic aberration which limit the spatial resolution. These are generally included by a non-linear contrast transfer function involving an integration in the diffraction plane [18–20], but a more useful representation for our purposes can be obtained by a real space formulation. Writing $\psi(r)$ for the electron wave after the specimen, $I(r)$ for the image intensity and expanding $\psi(r)$ about the diffraction g vectors as

$$\psi(r) = \sum_g \phi_g(r) \exp[-2\pi i(\chi + g)\cdot r],$$

then to a good approximation [26]

$$I(r) = \sum_{g \cdot q} \left[\phi_g(r) \otimes A_{g,q}(r)\right]\left[\phi_q(r) \otimes A_{q,g}(r)\right]^* \exp[-2\pi i(g - q)\cdot r],$$

where $\otimes$ stands for a convolution. For a perfect microscope, $A_{g.q}(r)$ would be a delta function whereas in practise the modulation terms $\phi_g(r)$ (which contain the information of interest) are averaged over position.

The effects arising are relatively complicated. Two terms contribute to $A_{g.q}(r)$, a long range oscillatory term and a damping term due to chromatic aberrations and the incident beam convergence. ($A_{g.q}(r)$ can be functionally approximated as the convolution of a real and an imaginary Gaussian.) If the damping is small, long range oscillations occur outside the edge, essentially the standard Fresnel effect. If instead the damping is large, the edge will be smeared over a large region (for instance 1 nm) and hence poorly resolved. For a clean surface image it is necessary to balance the two effects, damping out the oscillations whilst retaining a strongly peaked $A_{g.q}(r)$ in order to localise the information in the image. One free variable is the objective lens defocus which can be adjusted to achieve the "optimum" image. For the microscope employed and the gold spacings localised images are obtained for defoci of about -55 nm where the atomic columns are black, and also to a slightly lesser degree for defoci of about -100 nm contrast reversed so that the atomic columns are white, in both cases the focus tolerance being about ± 10 nm. We will refer to these defoci hereafter as those for "black dot" and "white dot" contrast respectively. Away from these defoci, even though the scattering may correspond to a column approximation, the electron optical imaging makes such an approximation untenable.

Three illustrations of the role of localisation for surface images are shown in figs. 3–5. Figs. 3a and 3b show experimental images of a gold (100) surface at defoci of approximately -25 and -55 nm respectively. Some surface disturbances are apparent for the black dot defocus of fig. 3b (whose structural significance is currently being investigated) which have been averaged out in fig. 3a. This illustrates the role of defocus. The effect of Fresnel oscillations outside a surface is shown in fig. 4 for calculated images of a vacancy column at a (111) surface for a focal spread halfwidth of 16 nm (Gaussian halfwidth)
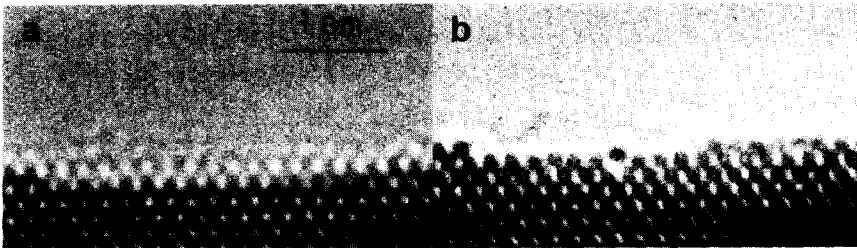

Fig. 3. Experimental images from a gold (100) surface illustrating the effect of objective lens defocus, in (a) -25 nm and (b) -55 nm.
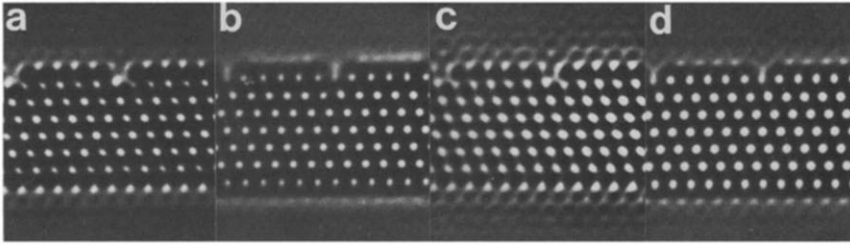
Fig. 4. Calculated images for a vacancy column to show the effect of Fresnel-like oscillations in confusing surface detail.

in figs. 4a and 4b and with no focal spread in figs. 4c and 4d. In both cases an aperture has been employed to exclude spacings less than 0.18 nm. The additional oscillations without the chromatic damping obscure the vacancy in figs. 4c and 4d. Fig. 5 illustrates the smearing of a surface when the damping term dominates. This experimental image is from an icosahedral multiply-twinned particle [26], and shows crossed (220) fringes of spacing 0.145 nm. (The results described herein were obtained using the (111) and (200) lattice fringes which have substantially larger spacings of 0.235 and 0.205 nm respectively, and for which the damping term was far smaller.)
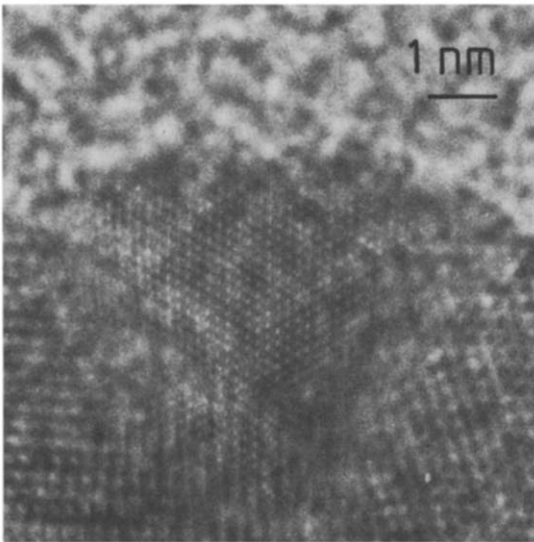

Fig. 5. Experimental image from a (111) oriented area of a small icosahedral particle. The microscope used has a large damping envelope for these spacings, so the surface cannot be cleanly imaged.

4. Surface imaging

Where direct imaging can provide important results is for surfaces which are not simple terminations of the bulk structure, but instead contain surface relaxations, reconstructions or impurities whose magnitude or nature are locally varying. It is convenient to sub-divide these structural modifications into two classes. Firstly there are variations in the surface potential or surface relaxations where the in-plane atomic structure of the surface is the same as the bulk. For these, detailed digital comparisons between experimental and theoretical images are essential. Secondly, there are more massive structural alterations such as reconstructions, surface steps and impurities where qualitative theory–experiment comparisons may be adequate.

One severe limitation of the grazing incidence technique discussed herein would be pointed out before proceeding further, namely the poor resolution attainable down the beam direction. Inhomogeneities along this direction are almost unobservable, although it is possible to estimate their extent from those in the image plane. An illustration of this ambiguity is shown in fig. 6. To the left the calculation has been carried out for a gold surface with a few single atom vacancies in the surface, on the right for surface interstitials (i.e. atoms outside the surface). The interstitials outside the main surface are clearly observable, but the vacancies cannot be detected.

4.1. Surface potentials

The simplest possible surface alteration is the surface potential. For high energy electrons there are contributions from both the static penetration of the valence electrons from the bulk into the surrounding medium and the dynamic electrostatic interactions between the electron beam and the conduction electrons inside the crystal. Within a classical model the second effect (the image force for fast electrons, see for instance ref. [27]) leads to both an elastic contribution and an inelastic component, the latter producing surface plasmon losses. These extend well out from the crystal surface, for instance at least 2 nm from the surface of a 100 nm cube of MgO [28,29].

The obvious question is whether a surface potential including such phenomena as Friedel oscillations is important for image contrast, and for a heavy element the calculations indicated that it was not. Images calculated with a large decaying surface potential (total height 10 eV/Å^3) with or without a complex component of 10% produced no discernible effect for thin crystals. As a cross-check, direct imaging of the plasmon losses from gold particles in a scanning transmission microscope at 100 kV did not show the large surface inelastic signal that has been observed for MgO [28,29]. We would expect that only for a material of low atomic number will a surface potential produce noticeable effects.
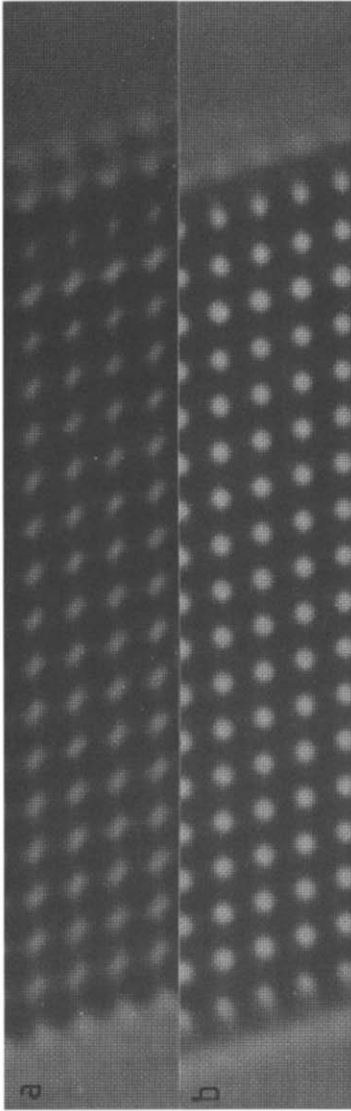
Fig. 6. Calculated images for vacancy and insterstitial surface defects, (a) for black dot contrast and (b) for white dot. On the left (vacancy) there are 18% fewer atoms in the surface layer, to the right (interstitial) an extra 18% outside the surface. The poor visibility of the extra atoms for the white dot contrast should be noted.
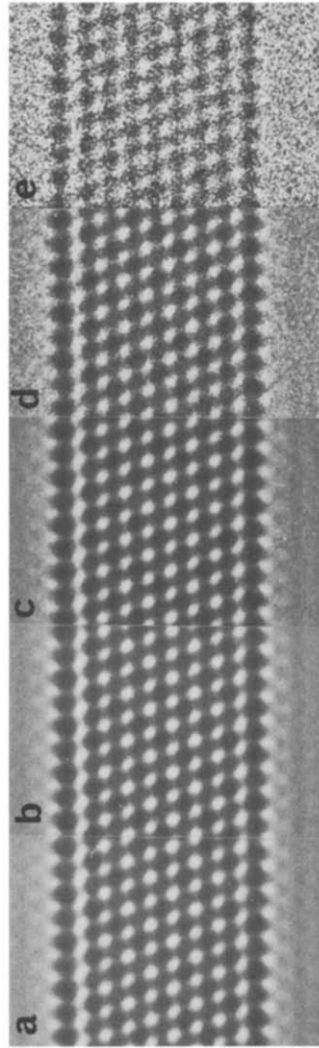
Fig. 7. The effect of shot noise on the clarity of an image, in sequence (a)–(e) with electron doses of ∞, 10^6, 10^5, 10^4 and 10^3 e·Å^{-2}. Particularly in (d) and (e) noise will severely limit precise measurements of any apparent relaxations. The loss in visibility of the Fresnel oscillations and the obscuring of a large structural relaxation (15% outwards) at the top surface should be noted.

4.2. Surface relaxations

The main problem with quantification of any surface relaxations is noise, both from any background support and statistical noise. Taking an electron exposure on the photographic emulsion of 1 electron/μm, an electron-optical magnification of 5×10^5, digital sampling using pixels of side 25 μm and a contrast level of 10%, then the ratio of contrast variations to statistical noise is 2.5:1. The effect of shot noise is shown for reference in fig. 7. Hence any attempt to measure fringe spacings to 25 μm or better on the photographic negative (0.5 Å) requires some form of lattice averaging to reduce the statistical noise. (In general we have worked with higher magnifications of between 7.5×10^5 and 10^5, although an alternative would be to employ a slower film.) Background noise from the substrate (typically amorphous carbon) is substantially coarser, producing contrast variations on a 3–5 Å scale dependent upon the electron-optical characteristics of the microscope. Typically one unit cell in the image will appear lighter or darker than its neighbours. These effects can also be removed by a translational average along the surface. Averaging procedures are well established (e.g. ref. [30]) and have been employed in work on gold (110) surfaces [9]. Because of these problems with noise and also the finite size numerical sampling, an uncertainty of 5% was estimated as the error bar for measurements of surface relaxations. (In principle, if a large and flat area of surface is available considerably smaller error bars might be achieved, but as yet no such experimental images are available; almost every surface that we have examined to date has shown marked local variations in the surface relaxations. In addition, the atoms on the surface were mobile, moving with velocities of the order of 1 Å s^{-1} (12).)

To interpret any surface relaxations, it is necessary to calibrate the behaviour of the system of interest by calculations for a range of structural relaxations. It is particularly important to choose the correct defocus, in our experiments the black dot defocus. (Away from this defocus the images were very insensitive to any surface relaxations.) At this defocus, the relationship of the apparent relaxations to structural relaxations is almost linear, as shown in fig. 8. To a good approximation, at 500 kV the experimental observation is 5% larger than the true structural relaxation. We note that this calibration curve was essentially independent of small variations in the defocus, spherical aberration, chromatic aberrations, beam convergence, and electron beam voltage.

4.3. Surface reconstructions

Structural variations where the surface periodicity is broken is an area where direct imaging is at its most powerful. Provided that black or white "dots" in the image are not over-interpreted, but are taken to indicate only the
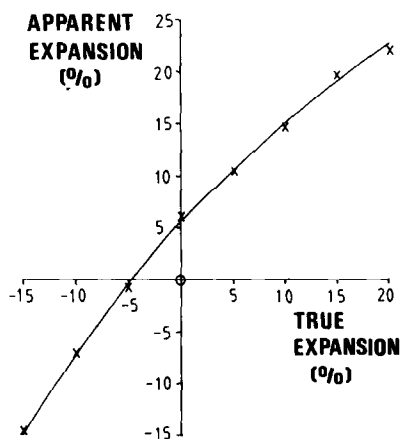
Fig. 8. Calculated relationship between apparent relaxation in the image with the structural relaxations for a gold (111) surface. There is some scatter of the data away from a smooth line due to the finite pixel size in the computations.

relative positions of the unit cells, and not their absolute locations, the image can be interpreted without detailed image simulations. (With the caution concerning localisation of the images detailed in section 3.) Surface steps and surface reconstructions such as the 2×1 (110) Au structure (ref. [9] and fig. 1) can be observed without complications. Discrimination between different models for a reconstruction can be absolute; by inspection the 2×1 surface of fig. 1 cannot be interpreted in terms of a surface buckle.

4.4. Surface impurities

Detecting and interpreting an impurity surface structure solely from high resolution images is possible, but can be very difficult in practice. There are two questions of importance, firstly the structure of the impurity layer, and secondly the chemical composition.

The local structure and substrate registry can normally be directly interpreted. For example, fig. 9 shows a simulation with an ordered carbon overlay on gold (111) in two different locations. (It should be noted that for the black dot contrast the carbon cannot be distinguished from the gold.) Differentiating between elements on a surface requires very careful analyses of images at different defoci. The characteristic feature is a different, qualitative contrast at the surface compared to a surface with the bulk chemical composition. An illustration of this technique is shown in fig. 10 for a gold (111) surface with a partially ordered molecular benzene overlay. Whilst at the black dot defocus the benzene and gold are similar, for the white dot defocus the benzene shows minimal contrast. (The experimental origin of this superstructure will be
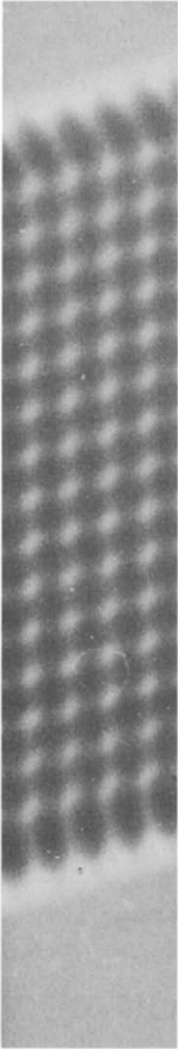
Fig. 9. Image simulation for a black dot contrast of surface carbon atoms either in line with the gold (left) or in between (right).
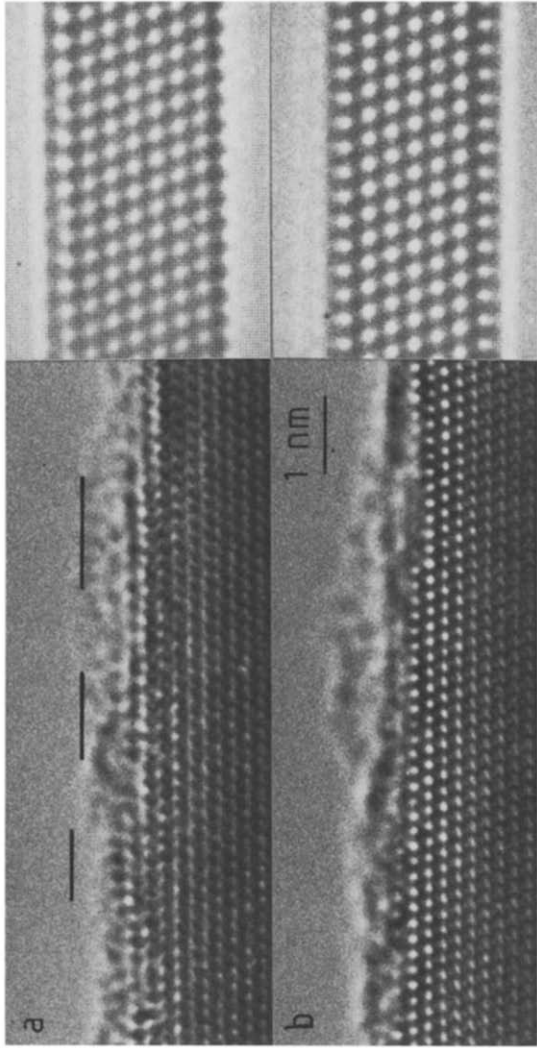

Fig. 10. Experimental (left) and calculated (right) images of a molecular benzene overlayer (in the regions marked) for black dot contrast in (a) and white dot contrast in (b). The benzene overlay is on the upper surface of the simulations only.

described elsewhere [13].) This technique will work if the scattering of the elements is very different, e.g. gold and carbon as described below, but if they are similar such as silver and gold it will probably fail. Experimentally it proved impossible to differentiate between these two elements in small particles of gold covered by evaporation with a thin coating of silver.

The nature of the contrast in fig. 10 for the black dot defocus is complicated. The benzene layer (a molecular hexagonal monolayer separated by Van der Waals radii) has a relatively strongly scattering spacing at about 2.8 Å, with the region between this layer and the gold substrate showing localised moire fringes. The form of the black lines connecting the two layers is very sensitive to the spacings of the superstructure. For instance, a graphitic layer would show a strong black line outside the gold connected to the substrate by weak lines with the bulk gold spacings. Such moire fringes should be generally useful for decoding the structure of surface adlayers.

5. Thicker specimens

The preceding sections have dealt with surface imaging where the thickness is relatively small (< 10 nm), and the image is formed primarily by electrons transmitted through the crystal with very little cross-talk between different columns of atoms. A different class of high resolution images can be expected for somewhat thicker particles where a large contribution to the scattering comes from electrons either reflected from the surface, diffracted initially inside the crystal and then escaping from the surface into the non-scattering vacuum outside, or if the crystal is tilted away from the zone axis so that the column approximation breaks down. (Crystal tilt is more important for thick than thin specimens.) A number of rather different and possibly misleading effects can occur, and we include here a short qualitative analysis in an attempt to short-circuit erroneous interpretations.

Particularly in a thicker specimen, the electron intensity inside the crystal will be attenuated by inelastic scattering processes, whereas any which escapes out of the surface will suffer considerably less attenuation. This can lead to images where the bulk shows low contrast with one or two high contrast surface layers or perhaps strong contrast outside the surface. An illustration of the latter is shown in fig. 11. One particularly unusual effect can occur if there is a thickness gradient along the surface traversing the thickness for an extinction. It is known from standard dynamical theory (e.g. ref. [23]) that there is often a phase shift of $\pi/2$ across an extinction contour. If on one side of the extinction thickness the image shows black contrast at the atomic sites, on the other it will show white contrast. Since the image is necessarily continuous, the bright surface layer will show complicated and artificial surface distortions as shown in fig. 12.
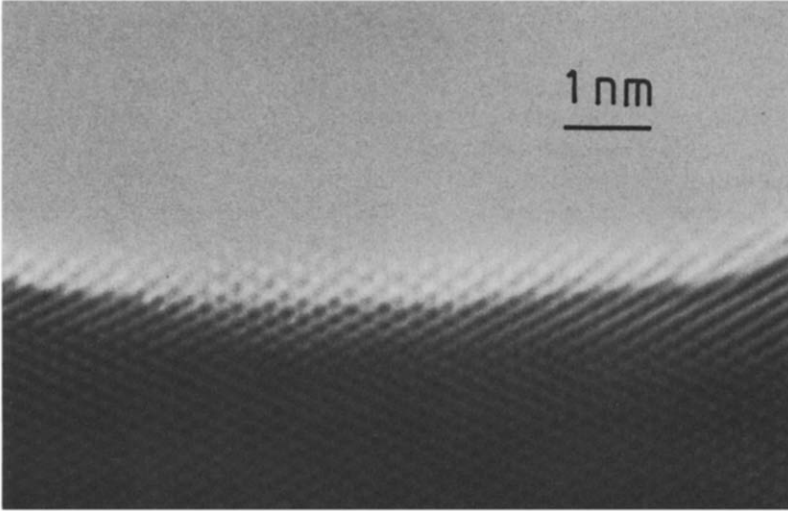
Fig. 11. Area of thick gold (110) surface showing strong fringe structure outside the surface here attributable to beam diffusion away from the edge. (The thickness is estimated at 25 nm.)
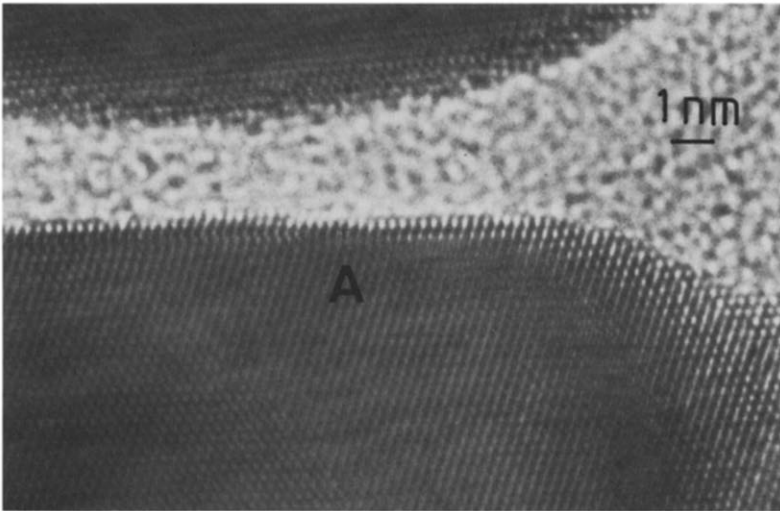
Fig. 12. Experimental image showing the confusing effects when an extinction contour meets a surface, particularly near "A".

6. Discussion

In the preceding sections some of the more important aspects of interpreting surface structure iamges have been described. We have deliberately only

considered the experimental results simultaneously with the theoretical calcula-
tions, since by experience synergistic application of the two is the correct
approach. We have also not included any discussion of possible complications
such as inelastic scattering (excepting the surface potential in section 4.1 and
for thicker specimens in section 5); calculations with imaginary components to
the potential implies that down the zone axis these were not crucial to the
interpretation. Also more complicated shapes for the crystals such as inclined
faces away from the surface have not been discussed – these also were found to
be unimportant (down the zone axis). The general conclusion is that interpreta-
tion is quite simple, once the characteristics of the system are understood.
Indeed, most of the images can be interpreted by a column approximation
equivalent to a projection of the crystal structure down the beam direction.
The fact that this approximation is so good makes the technique one of
considerable promise. The problem is to obtain imaging conditions which fulfil
the column approximation.

Comparable results can certainly be expected for other metals and less
powerful electron microscopes. Metals adjacent to gold in the periodic table
(such as platinum) have similar lattice structures and scattering potentials, and
their images are (from preliminary calculations) almost identical. Preliminary
experimental results for a platinum on charcoal catalyst by Noordally and
Freeman [31] and silver catalyst by Wheatley et al. [32] show the atomic
surface structure. Possible complications due to unknown surface impurities is
a problem which will hopefully be solved in the near future with the use of
UHV microscopes. Applications of the techniques both in pure surface science,
and in examining the surfaces of catalytic metal particles should provide
extensive new data. High voltage machines may be required for thicker sample
surface science, but current commercial 200 kV microscopes should be ade-
quate for thin samples such as heterogeneous metal catalyst particles. However,
one limitation of the technique compared to LEED and RHEED may be
insoluble, namely the problem of electron beam damage; with the high beam
currents normally employed most loosely bound impurities will probably
desorb. Hence many overlay structures may not be accessible.

It is appropriate to conclude with the comment that other transmission
electron microscope techniques should be equally capable of providing useful
information. Reflection techniques and surface sensitive diffracted beams have
already been employed (e.g. refs. [1–3]), as mentioned in the introduction.
Some initial results (e.g. refs. [33,34]) have provided useful two-dimensional
data by high resolution imaging normal to the surface of interest. However,
this approach is considerably more susceptible to contamination artefacts than
the grazing incidence technique employed herein. With this normal incidence
technique the image shows only the projected structure of *both* surface and
bulk materials, and the presence of one or two monolayers of a light element
contaminant such as carbon would not effect the image. In contrast the grazing

incidence technique is strictly monolayer sensitive, with surface impurities, if present, clearly observable. Other lower resolution techniques should also prove useful. For instance, dark field techniques should be very sensitive to any strain fields associated with surface buckling. Microdiffraction (e.g. ref. [35]) should also prove useful as local RHEED patterns are available, and surface microanalytical techniques in a scanning electron microscope (e.g. ref. [36]) employing electron energy loss, X-ray and Auger signals should be capable of providing extensive, local elemental information from inhomogeneous samples.

Acknowledgements

Appendix

The intention of this section is to describe briefly the algorithm employed for the numerical multislice integration utilising virtual memory array storage. The aim is to minimise non-sequential array access which can be exceedingly expensive in computer time. We assume here one fairly large in-core buffer, a basic acquaintance with the multislice technique utilising Fast Fourier Transforms (e.g. ref. [16]) and also that the wavefunction in reciprocal space is only calculated for values between H1, H2 along the rows and K1, K2 down the columns (to avoid aliasing). The algorithm for a single slice is shown schematically in fig. 13, employing one-dimensional Fast Fourier Transforms, with m being the number of columns that can be accommodated in the buffer. The slow step is the central column transfer and Fourier Transform section. This consists of two arrayed transposes, here by a simple buffered array method although an approach based upon the method of Singleton [37] might be more efficient. The speed of the algorithm will depend upon the efficiency of the virtual memory system and the size of the buffer, but as a reasonable estimate is 2–3 times slower than an in-core multislice calculation.
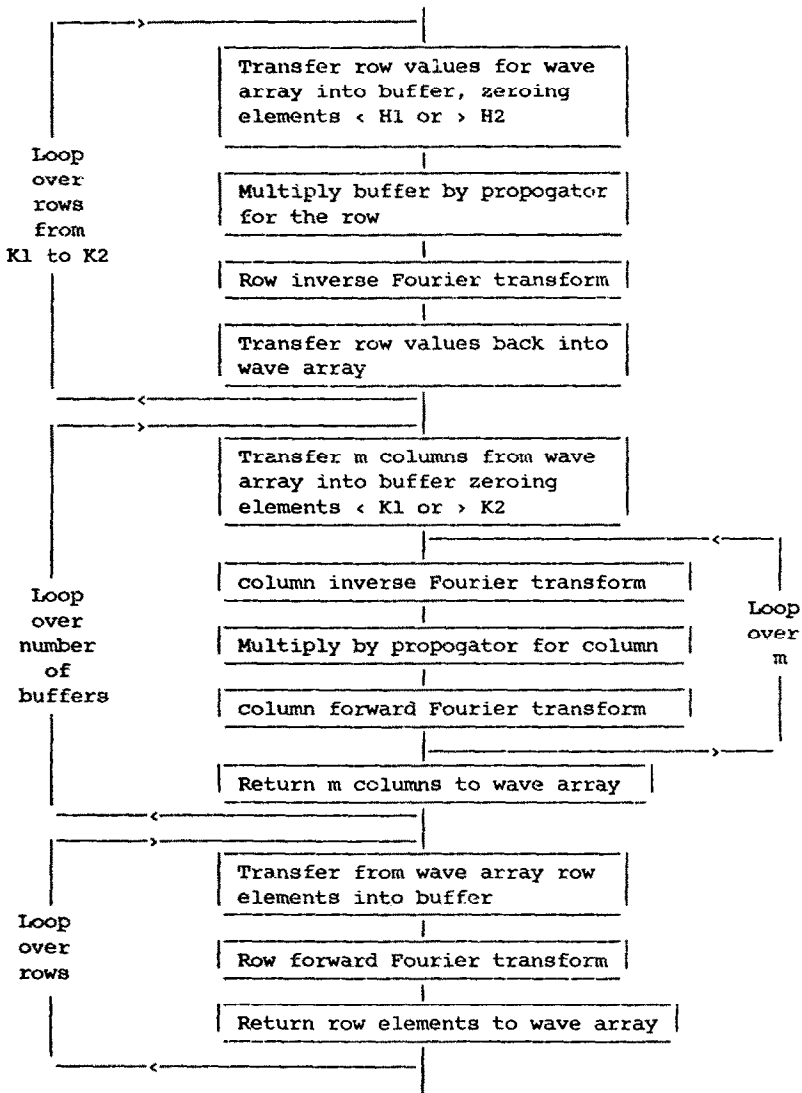
```
┌──────>─────────────────────┐
│                            │ Transfer row values for wave
│                            │ array into buffer, zeroing
│                            │ elements < H1 or > H2
│  Loop                      ├───────────────────────────
│  over                      │ Multiply buffer by propogator
│  rows                      │ for the row
│  from                      ├───────────────────────────
│  K1 to K2                  │ Row inverse Fourier transform
│                            ├───────────────────────────
│                            │ Transfer row values back into
│                            │ wave array
│  ─────────<────────────────┘
│  ─────────>─────────────────┐
│                            │ Transfer m columns from wave
│                            │ array into buffer zeroing
│                            │ elements < K1 or > K2
│                            ├──────────────────────<──┐
│  Loop                      │ column inverse Fourier transform   │
│  over                      ├───────────────────────────  Loop
│  number                    │ Multiply by propogator for column  over
│  of                        ├───────────────────────────   m
│  buffers                   │ column forward Fourier transform   │
│                            ├──────────────────────>──┘
│                            │ Return m columns to wave array
│  ─────────<────────────────┘
│  ─────────>─────────────────┐
│                            │ Transfer from wave array row
│                            │ elements into buffer
│  Loop                      ├───────────────────────────
│  over                      │ Row forward Fourier transform
│  rows                      ├───────────────────────────
│                            │ Return row elements to wave array
│  ─────────<────────────────┘
```

Fig. 13. Virtual memory algorithm used for the calculations.

Note added in proof

Following acceptance of this paper, some unrelated theoretical work dealing with a wavepacket treatment of electron diffraction confirmed the validity of a column approximation for surfaces. When imaged exactly down a zone axis orientation, the approximation holds well for high energy electrons and a

strong scatterer such as gold. However, for a weak potential, lower voltages or small tilts off the zone axis it will break down.

References

[1] N. Osakabe, Y. Tanishiro, K. Yagi and G. Honjo, Surface Sci. 97 (1980) 393.
[2] N. Osakabe, Y. Tanishiro, K. Yagi and G. Honjo, Surface Sci. 109 (1981) 353.
[3] Y. Tanishiro, H. Kanamori, K. Takayana, K. Yagi and G. Honjo, Surface Sci. 111 (1981) 395.
[4] D.J. Smith, Helv. Phys. Acta 56 (1983) 464.
[5] J.C.H. Spence, Experimental High Resolution Electron Microscopy (Oxford University Press, 1981).
[6] S. Iijima, Chem. Scripta 14 (1978–79) 117.
[7] J.V. Sanders, Chem. Scripta 14 (1978–79) 141.
[8] L.D. Marks and D.J. Smith, Nature 303 (1983) 316.
[9] L.D. Marks, Phys. Rev. Letters 51 (1983) 1000.
[10] D.J. Smith and L.D. Marks, in: Proc. 7th Intern. Conf. on High Voltage Electron Microscopy, Berkeley, CA, 1983.
[11] L.D. Marks, V. Heine and D.J. Smith, Phys. Rev. Letters, submitted.
[12] D.J. Smith and L.D. Marks, in preparation.
[13] L.D. Marks and D.J. Smith, in preparation.
[14] J.M. Cowley and A.F. Moodie, Acta Cryst. 10 (1967) 609.
[15] P. Goodman and A.F. Moodie, Acta Cryst. A30 (1974) 280.
[16] P.G. Self, M.A. O'Keefe, P.R. Buseck and A.E.C. Spargo, Ultramicroscopy 11 (1983) 35.
[17] D.J. Smith, R.A. Camps, L.A. Freeman, R. Hill, W.C. Nixon and K.C.A. Smith, J. Microscopy 130 (1983) 127.
[18] M.A. O'Keefe, in: Proc. 37th Annual EMSA Meeting, San Antonio, TX, 1979 (Claitor's, Baton Rouge, LA, 1979) p. 556.
[19] W.O. Saxton, J. Micros. Spectrosc. Electron. 5 (1980) 661.
[20] K. Ishizuki, Ultramicroscopy 5 (1980) 55.
[21] J.W. Cooley and J.W. Tukey, Math. Compt. 19 (1965) 297.
[22] P.B. Hirsch, A. Howie, R.B. Nicholson, D.W. Pashley and M.J. Whelan, Electron Microscopy of Thin Crystals (Butterworths, London, 1965).
[23] A. Howie and Z.S. Basinski, Phil. Mag. 149 (1969) 1039.
[24] M.V. Berry, J. Phys. C4 (1971) 697.
[25] L.D. Marks, Ultramicroscopy 12 (1983–84) 237.
[26] L.D. Marks and D.J. Smith, J. Crystal Growth 54 (1981) 425.
[27] A. Howie, Ultramicroscopy 11 (1983) 141.
[28] L.D. Marks, Inst. Phys. Conf. Ser. 61 (1981) 473.
[29] L.D. Marks, Solid State Commun. 43 (1982) 727.
[30] J. Frank, in: Computer Processing of Electron Microscope Images, Ed. P.W. Hawkes (Springer, Berlin, 1980) p. 245.
[31] E. Noordally and L.A. Freeman, personal communication.
[32] D. Wheatley, L.A. Freeman and A. Howie, personal communcation.
[33] K. Takanayagi, K. Kobayashi, K. Kodaira, Y. Yokoyama and K. Yagi, in: Proc. 7th Intern. Conf. on High Voltage Electron Microscopy, Berkeley, CA, 1983.
[34] G. Nihoul, K. Abdelmoula and J.J. Métois, Ultramicroscopy 12 (1983–84) 353.
[35] J.M. Cowley, in: Scanning Electron Microscopy 1982, Anaheim, CA, Ed. O. Johari (SEM, AMF O'Hare, IL, 1982).
[36] D.I. Wheatley and A. Howie, in: Proc. EMAG 1983, Guildford, UK, in press.
[37] R.C. Singleton, IEEE Trans. Audio Electroacoust. AU-15 (1967) 91.